Space- and time-resolved UV-to-NIR surface spectroscopy and 2D nanoscopy at 1 MHz repetition rate

Bernhard Huber[1], Sebastian Pres[1], Emanuel Wittmann[2], Lysanne Dietrich[1], Julian Lüttig[1], Daniel Fersch[1], Enno Krauss[3], Daniel Friedrich[3], Johannes Kern[4], Victor Lisinetskii[1], Matthias Hensen[1], Bert Hecht[3], Rudolf Bratschitsch[4], Eberhard Riedle[2], and Tobias Brixner[1,5,]*

[1] Institut für Physikalische und Theoretische Chemie, Universität Würzburg, Am Hubland, 97074 Würzburg, Germany

[2] Lehrstuhl für BioMolekulare Optik, Ludwig-Maximilians-Universität München, Oettingenstrasse 67, 80538 München, Germany

[3] NanoOptics & Biophotonics Group, Experimental Physics 5, Universität Würzburg, Am Hubland, 97074 Würzburg, Germany

[4] Institute of Physics and Center for Nanotechnology, University of Münster, Wilhelm-Klemm-Str. 10, 48149 Münster, Germany

[5] Center for Nanosystems Chemistry (CNC), Universität Würzburg, Theodor-Boveri-Weg, 97074 Würzburg, Germany

*Corresponding author: Tobias Brixner, brixner@phys-chemie.uni-wuerzburg.de

Review of Scientific Instruments

ABSTRACT: We describe a setup for time-resolved photoemission electron microscopy (TR-PEEM) with aberration correction enabling 3 nm spatial resolution and sub-20 fs temporal resolution. The latter is realized by our development of a widely tunable (215–970 nm) noncollinear optical parametric amplifier (NOPA) at 1 MHz repetition rate. We discuss several exemplary applications. Efficient photoemission from plasmonic Au nanoresonators is investigated with phase-coherent pulse pairs from an actively stabilized interferometer. More complex excitation fields are created with a liquid-crystal-based pulse shaper enabling amplitude and phase shaping of NOPA pulses with spectral components from 600 to 800 nm. With this system we demonstrate spectroscopy within a single plasmonic nanoslit resonator by spectral amplitude shaping and investigate the local field dynamics with coherent two-dimensional (2D) spectroscopy at the nanometer length scale ("2D nanoscopy"). We show that the local response varies across a distance as small as 33 nm in our sample. Further, we report two-color pump–probe experiments using two independent NOPA beamlines. We extract local variations of the excited-state dynamics of a monolayered 2D material (WSe_2) that we correlate with low-energy electron microscopy (LEEM) and reflectivity (LEER) measurements. Finally, we demonstrate the in-situ sample preparation capabilities for organic thin films and their characterization via spatially resolved electron diffraction and dark-field LEEM.

I. INTRODUCTION

Coherence effects lie at the heart of many phenomena observed in physics and chemistry.[1] In solids and on surfaces, strong interactions of the system with the environment typically lead to fast coherence decay. Thus, the observation of coherence phenomena on surfaces requires femtosecond time resolution, which is offered by ultrafast laser spectroscopy techniques. Another major challenge in disentangling the dynamics of heterogeneous or nanostructured materials aside from the required temporal resolution, is the limited spatial resolution due to the optical diffraction limit. A solution is offered by time-resolved photoemission electron microscopy (TR-PEEM) that combines ultrafast optical excitation and high-resolution photoelectron imaging capabilities. This method is perfectly suited for the investigation of dynamical phenomena on the nanometer length and femtosecond time scale.

The spatial resolution of PEEM is fundamentally limited by the de Broglie wavelength of the photoemitted electrons in the range of 1 nm. In practice, the achievable resolution is limited by spherical and chromatic aberrations in the electron imaging lens system[2–4] and space-charge effects, depending on the used illumination source.[5] Using a mirror aberration corrector, the impact of aberration effects is minimized and a spatial resolution of 3 nm and smaller can be achieved in commercially available PEEM devices. For TR-PEEM, Ti:Sapphire oscillator lasers are the most common source for ultrashort excitation pulses.[6–11] This is because oscillator systems with repetition rates on the order of 80 MHz and pulse energies in the few-nJ regime offer high average count rates for imaging while the number of generated photoelectrons per laser pulse is low enough to avoid image distortions due to space-charge effects.[12,13] Broadband pulses of < 10 fs temporal duration provide superior time resolution for pump–probe experiments. On the downside,

Ti:Sapphire oscillator lasers offer only limited wavelength tunability as they are typically centered around 800 nm, and higher photon energies are obtained by frequency doubling or tripling.

Synchronously pumped optical parametric oscillators provide increased wavelength flexibility in the visible (VIS) and infrared spectral region, but the ultrafast time resolution is typically lost and pulse energies are limited to sub-10 nJ, which inhibits efficient third- or higher-order photoemission processes. High-harmonic generation (HHG) in noble-gas jets results in pulses with photon energies up to 100 eV and ~100 as pulse durations as employed for core-level electron microscopy in an optical-pump–extreme-ultraviolet-probe scheme.[14–16] While these systems offer an unmatched temporal resolution, low repetition rates of a few kHz lead to extensive exposure times at flux densities low enough to minimize imaging distortions due to space-charge effects. To date, the development of high-repetitive sources of attosecond pulses for time-resolved spectroscopy and microscopy is an ongoing effort with first results at 200 kHz.[17] A noncollinear optical parametric amplifier (NOPA) is capable of combining the design paradigms of broadband pulses with a wide-ranging flexibility of central wavelengths from the near-infrared (NIR) to the ultraviolet (UV) regime as well as high (MHz) repetition rates for time-resolved spectro-microscopy.[18–20] First laser-excited PEEM experiments using a MHz-NOPA were demonstrated by Höfer[20] and the technique was since applied for ultrafast photoemission imaging of plasmonic modes in nanostructured materials[22,23] and ferroelectric domains.[24] Moreover, high-repetition rate NOPA systems were also used in spatially averaged time-resolved photoemission experiments.[25,26]

In this work, we describe our experimental setup that combines aberration-corrected PEEM with a broadband-tunable (215–970 nm) NOPA system at 1 MHz repetition rate for ultrafast pump–

probe imaging and coherent multidimensional spectroscopy at the nano–femto scale. We realize 3 nm lateral resolution and sub-20 fs temporal resolution in combination with broadband pulse shaping. In previous work by some of us, we already introduced and applied photoelectron-detected coherent two-dimensional (2D) spectroscopy with spatial resolution, termed "coherent 2D nanoscopy".[27,28] The present work extends this method with broadband wavelength tunability of the exciting laser source and increased spatial resolution through aberration-corrected PEEM.

This paper is arranged as follows: In Section I, we provide an overview of the experimental apparatus and describe central features. In Section II, we discuss individual components and illustrate their function with exemplary experiments, specifically the NOPA setup (Section II.A), a phase-stable interferometer for coherent two-pulse experiments (Section II.B), pulse shaping for the realization of 2D spectroscopy (Section II.C), the PEEM itself (Section II.D), two-color experiments (Section II.E), low-energy electron microscopy (LEEM) and reflection (LEER) (Section II.F), and the preparation and characterization of organic samples (Section II.G). We summarize and conclude in Section III.

I. SETUP OVERVIEW

An overview scheme of the complete setup is shown in Fig. 1. A two-branch NOPA of our own design is pumped by an Yb-doped fiber laser (Amplitude Systèmes, Tangerine HP) at a central wavelength of 1030 nm, a pulse energy of 35 µJ and ~320 fs pulse duration at 1 MHz repetition rate. A half-wave plate in combination with a thin-film polarizer splits off a portion of the output beam and the resulting 20 µJ pulses pump the NOPA with two parallel amplification beamlines, generating tunable output pulses in the range of 400–670 nm (see ref. [20]) and 630–970 nm (ref. [29]),

while simultaneous operation of the two branches is possible (blue and red lines in Fig. 1, respectively). Broadband output pulses of 300–600 nJ are routinely compressed to sub-20 fs with separate prism compressors for each NOPA beamline. Frequency doubling in a very thin and properly oriented β-$BaBO_3$ (BBO) crystal of either NOPA beamline results in ~30 nJ pulses with a photon energy of up to 5.8 eV (corresponding to 215 nm), indicated as a purple line in Fig. 1 for one NOPA output. In combination, the laser system offers gap-less wavelength tunability ranging from the UV to the NIR at 1 MHz repetition rate.

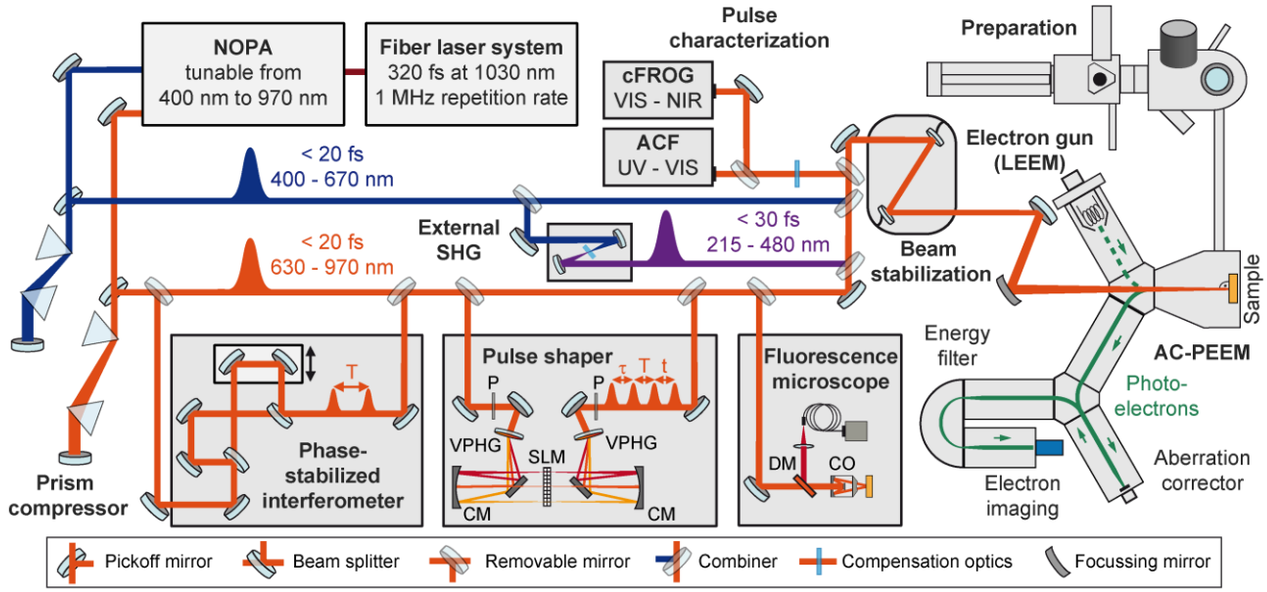

Fig. 1. Experimental setup for time-resolved photoemission electron microscopy (TR-PEEM). The noncollinear optical parametric amplifier (NOPA) pumped with Yb-doped fiber laser radiation renders broadband tunable pulses at 1 MHz repetition rate. Simultaneous emission of two independent output beams (red and blue solid lines) is possible and pulses are compressed with prism compressors to typically sub-20 fs. Second-harmonic generation (SHG) generates ultraviolet radiation with pulse energies up to 5.8 eV for efficient low-order photoemission. A Mach–Zehnder-type interferometer with active stabilization generates phase-coherent excitation pulse pairs with time delay *T* and a pulse shaper based on a liquid-crystal-display spatial light modulator (SLM) and volume phase holographic gratings (VPHG) enables tailored optical fields with full amplitude and phase control. Excitation pulse trains covering the range of 600–800 nm are available for multidimensional spectroscopy. NOPA output pulses are combined and guided to the

aberration-corrected electron microscope via an active beam stabilization or, alternatively, to the pulse characterization setup consisting of autocorrelators (ACF) and collinear frequency-resolved optical gating (cFROG). Electrons photoemitted from the sample are guided, energy-filtered and imaged with high spatial resolution down to 3 nm. The system is complemented with a two-part preparation and characterization UHV chamber as well as a scanning fluorescence microscope with a Cassegrain-type reflective objective (CO) to minimize dispersion, a dichroic mirror (DM) for signal filtering, and fluorescence lock-in detection with an avalanche photodiode.

The simultaneous operation of the two NOPA beamlines enables time-resolved two-color pump–probe experiments, e.g., for resonant sample excitation with a pump pulse in the visible and subsequent photoemission with an UV probe pulse while the wavelength of either pulse may be chosen independently. For interferometric time-resolved photoemission experiments, phase-coherent pairs of time-delayed pump pulses are generated with an actively phase-stabilized Mach–Zehnder interferometer in the range of 440–970 nm. Further, we use a liquid-crystal-display-based spatial light modulator (LCD-SLM) in 4*f* geometry to generate tailored optical fields with simultaneous control of amplitude and phase.[30,31] To ensure a horizontal polarization at the LCD-SLM a polarizer P (Thorlabs, LPVIS050-MP2) at the beam input is used. The femtosecond pulse is spectrally decomposed by a transmittive volume phase holographic grating VPHG (Wasatch Photonics, 938 l/mm) and focused by a cylindrical protected silver mirror CM (Hellma Optics, R = -600 mm). The dual-layer 640-pixel LCD-SLM (Jenoptik, SLM-S640d USB) is directly placed in the Fourier plane and enables spectral phase control of each spectral component. Due to the symmetric pulse shaper geometry the shaped spectral components are reassembled and amplitude- and phase-shaped pulse sequences (e.g. four-pulse sequence with time delays τ, T, t) are generated behind the second horizontal polarizer P (Thorlabs, LPVIS050-MP2) and guided to the PEEM. In comparison to conventional LCD-SLM pulse shapers that are designed for a fixed input laser spectrum, the pulse shaper in our setup is covering a spectral region ranging from 600–800 nm

which enables pulse shaping of tunable NOPA output pulses with corresponding spectral components.

Both NOPA output beamlines are combined with a wavelength-adapted dichroic mirror (Laseroptik GmbH) and are guided to the PEEM. A commercial active beam stabilization (TEM Messtechnik GmbH, Aligna 4D) corrects for vibrational instabilities between the optical table and the ultrahigh-vacuum (UHV) chamber of the PEEM. Sample illumination is possible in normal incidence (90°) or under gracing incidence (16°) to the sample surface (not shown in Fig. 1) through fused-silica viewports of 1.5 mm thickness (Torr Scientific Ltd., VPZ16Q-LN) flanged to the electron microscope UHV chamber. For laser pulse characterization in the VIS and NIR, the beam is guided to a commercial autocorrelator setup in combination with frequency-resolved optical gating (APE GmbH, pulseCheck). UV pulse duration measurements are performed with an autocorrelator of our own design, based on bulk-material two-photon absorption. The packaged unit is based on the demonstrations by Homann *et al*.[32] For dispersion matching, pulse propagation lengths and transmissive optics in the characterization beam path resemble the PEEM experimental conditions.

For metallic and molecular thin-film preparation and characterization, an additional two-part UHV preparation chamber is attached to the main PEEM chamber. Further, a self-constructed scanning fluorescence microscope with an all-reflective objective complements the PEEM setup for correlative space- and time-resolved experiments, sample pre-characterization, and comparative (2D) spectroscopy evaluation with complementary (fluorescence) lock-in detected observables.[33]

II. SETUP COMPONENTS AND EXEMPLARY APPLICATIONS

A. Noncollinear optical parametric amplifier (NOPA)

The scheme of the two-branch NOPA is shown in Fig. 2a and is based on the concept introduced by Bradler *et al*.[20] A portion of 20% of the pump radiation is used for the generation of two supercontinua from the fundamental (1ω SCG) and second harmonic (2ω SCG) of the pump in 4 mm YAG crystals, serving as seeds for the two NOPA branches. The remaining part of the 1030 nm pump radiation is converted to its second (2ω) and third harmonic (3ω) in an all-collinear geometry for the amplification of selected spectral parts of the seed lights. Opposed to previous implementations with lower pump pulse energies[19–21], in our setup a novel concept reducing two-photon absorption-induced heating in the BBO crystals is applied in order to avoid pulse energy instabilities.[34] A custom-designed α-BBO plate in front of the 3ω-generating crystal compensates for the relative time delays of the fundamental and 2ω pulse and shifts the temporal overlap of the pulses towards the exit facet of the 3ω crystal and thus the location of UV light generation. This minimizes the UV pulse propagation inside the crystal and thus the build-up of heat due to two-photon absorption. Seed (1ω SCG and 2ω SCG) and amplification pulses (2ω and 3ω) are superimposed in the NOPA crystals, with exemplary output spectra shown in Fig. 2b (red and dark blue shading, respectively). With an additional SHG step of either NOPA output the tunability is extended to the UV and thus, in total, the source delivers broadband pulses covering a range of 215–970 nm central wavelength.

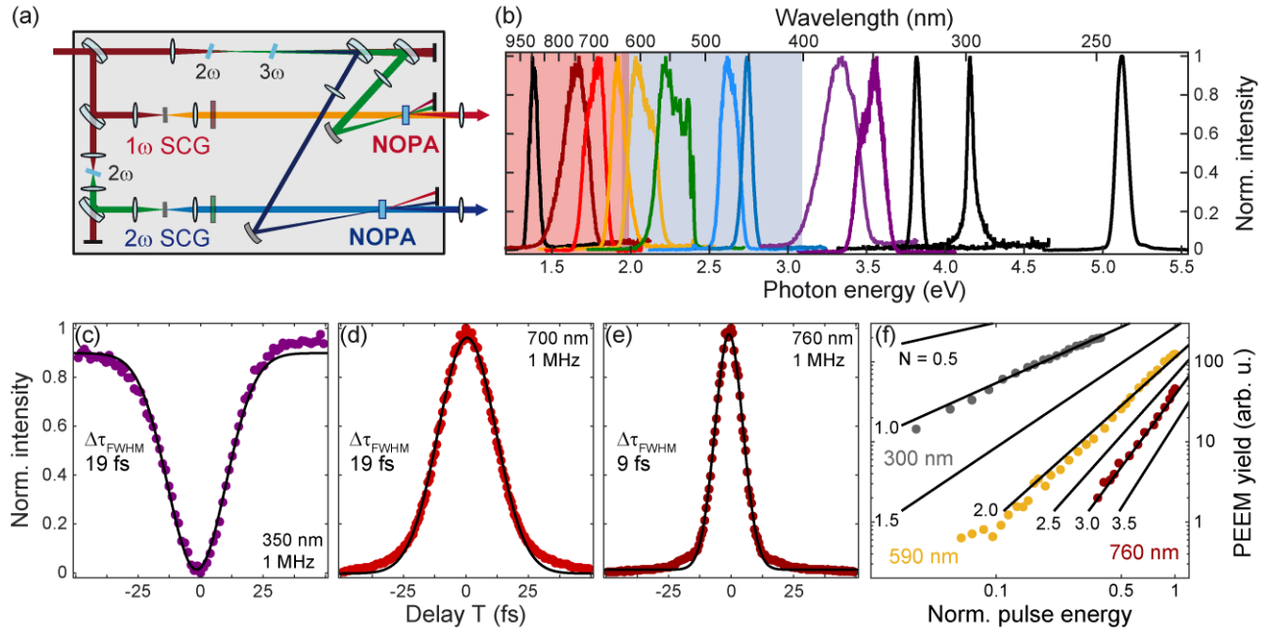

Fig. 2. Broadband tunable NOPA with two decoupled output branches. (a) Concept of the NOPA system: Generation of two continua (SCG) with the fundamental ($\boldsymbol{1\omega}$) and second harmonic ($\boldsymbol{2\omega}$) of an Yb-fiber input laser. Second ($\boldsymbol{2\omega}$) and third ($\boldsymbol{3\omega}$) harmonic pulses are generated consecutively and amplify broadband fractions of the $\boldsymbol{1\omega}$ SCG and $\boldsymbol{2\omega}$ SCG, respectively. (b) Exemplary NOPA output spectra ranging from the near-infrared to the ultraviolet (UV) spectral region. Color shading illustrates the tuning ranges of the NOPA branches seeded by the $\boldsymbol{1\omega}$ SCG (red) and the $\boldsymbol{2\omega}$ SCG (dark blue). Second-harmonic generation (SHG) of either output extends the tunability down to the UV. Output pulse durations are characterized with noncollinear intensity autocorrelation (c) using two-photon absorption in the UV around 350 nm and (d, e) using SHG in the visible and near-infrared, exemplarily shown around 700 nm (d) and 760 nm (e). From the full width at half maximum (FWHM) of Gaussian fits to the autocorrelation data, $\Delta\boldsymbol{\tau_{gauss}}$, the pulse durations are extracted ($\Delta\boldsymbol{\tau_{FWHM}} = \Delta\boldsymbol{\tau_{gauss}}/\boldsymbol{1.414}$). (f) Pulse energy dependence of the photoemission yield from a flat Ag(111) crystal surface with excitation wavelengths 300 nm (grey), 590 nm (yellow), and 760 nm (dark red) in normal-incidence illumination. Black lines indicate different power-law dependencies of increasing order *N*.

Figures 2c and 2d show the compressibility of pulses with a pair of Brewster-angle fused-silica prisms to sub-20 fs across the tuning range with shortest pulse durations of sub-10 fs demonstrated for 760 nm central wavelength in Fig. 2e. The sub-20 fs pulse duration of the frequency-doubled

UV pulse shown in Fig 2c was obtained by pre-compressing the fundamental pulse at 700 nm central wavelength with the prism compressor.[35] In the PEEM experiment, the choice of the excitation wavelength alters the order of the detected multiphoton absorption in the photoemission process. Further, efficient higher-order photoemission in the VIS is possible due to few-hundred nJ pulse energies and there is no need to reduce the sample work function or affinity with additional adsorbates such as Cs. Figure 2f shows the power-law dependence of the photoemission yield from a flat Ag(111) crystal surface as a function of the excitation pulse energy for the different center wavelengths 760 nm, 590 nm, and 300 nm (1.63 eV, 2.10 eV, and 4.13 eV, respectively). The comparison of the measured data with calculated orders N of the power-law dependency (black lines in Fig. 2f) indicates a decrease of the order of the photoemission process with increasing photon energy from $N = 3$ to 1. This graph exemplifies the usefulness of the broad wavelength tunability of the setup for photoemission experiments.

B. Phase-stable interferometer

For single-color pump–probe PEEM experiments, phase-coherent two-pulse sequences can be generated from setups using active[36,37] or passive[38,39] stabilization. In our setup presented here, an actively stabilized Mach–Zehnder-type interferometer is used to generate two identical pulses with a controllable inter-pulse time delay T, following the design of Wehner *et al*.[40] Active stabilization compensates for the differential drift of the two interferometer arms due to environmental disturbances during the TR-PEEM experiment which can last up to several hours, i.e., real-time compensation of changes in the path lengths with nanometer precision is necessary. The design, depicted in Fig. 3a, enables precise control of the inter-pulse time delay as well as continuous scanning. The incoming NOPA beam is divided into two parts of equal intensity with a broadband

beamsplitter (Layertec GmbH, 440–1020 nm, substrate thickness 1 mm), adapted to the wavelength tuning ranges of the NOPA output. The path length of one interferometer arm is controlled with a piezoelectric actuator (Newport Corp., NPX-400SG) and both arms are recombined with a combiner optic identical to the beamsplitter. The number of reflections and transmissions in both arms is balanced, while the 1 mm thickness of the beamsplitter/combiner minimizes the amount of dispersion. Parallel to the NOPA beam path, an intensity-stabilized HeNe laser (Thorlabs Inc., HRS015B) beam propagates through the interferometer and acts as a reference for active stabilization. A half-wave plate in the HeNe beam in one arm generates perpendicular linear polarizations that are converted to left- and right-circularly polarized light after recombination with a quarter-wave plate. Phase jitter due to length disturbances translates to a change of the orientation of the resulting linear sum polarization, which we detect with a combination of a polarizer and a photodiode. This signal is fed into a proportional–integral–derivative controller which generates a control signal acting on the piezo actuator, i.e., stabilizing the phase signal with a precision corresponding to $\pm$ 20 as pulse delay. In turn, motorized polarizer rotation (Owis GmbH, DRTM 65-D35-HiDS) induces a change of the detected photodiode signal which is compensated by the feedback loop with an introduced phase by the piezo actuator. In this way, e.g., a 360° polarizer rotation generates a time delay of 4.2 fs between pulses in the two interferometer arms.

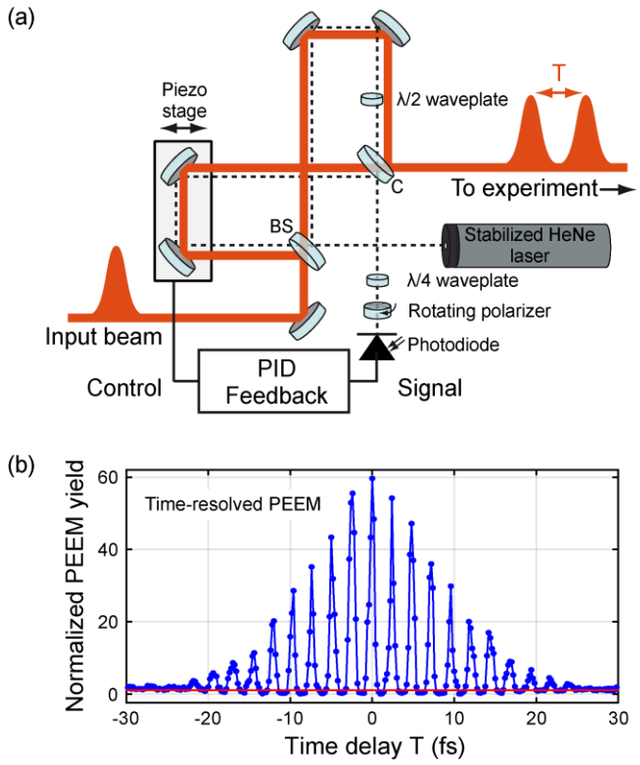

Fig. 3. Generation of phase-coherent pulse pairs with a Mach–Zehnder-type interferometer and active stabilization. (a) Setup scheme with the beam paths of NOPA in red and referencing continuous-wave helium–neon laser (HeNe) in dashed black. Time-dependent phase distortions in either arm of the interferometer are detected as signal input of a proportional–integral–derivative (PID) controller for active counter-control movement of a piezo-driven delay stage. Polarizer rotation corresponds to a change of the working setpoint of the PID loop and allows for the introduction of variable time delays *T*. (b) Time-resolved high-order (3.5) photoemission yield of Au nanorods with NOPA excitation (720 nm) in blue in steps of 200 as. The background signal for time delays $\boldsymbol{T > |\pm 50|}$ fs with well-separated pulses is indicated in red.

As an exemplary application, we performed phase-resolved interferometric TR-PEEM of commercial Au nanorods (Nanopartz Inc., E12-25-650-NPO-ETOH-50) on an indium–tin–oxide-covered glass substrate with pulses centered at 720 nm. Nanorod illumination with a polarization vector parallel to the rod axis excites a localized surface plasmon which gives rise to strong electromagnetic field concentration, predominantly at both ends of the Au rod. These “hot spots”

lead to an enhanced local photoemission yield through multiphoton absorption, which we detect with PEEM. The spatially averaged PEEM signal over such a photoemission hot-spot area is shown in Fig. 3b as a function of the inter-pulse delay T of the two-pulse sequence. The step size is $\Delta T = 200$ as, corresponding to 12 sampling points per period. This is necessary because the nonlinear behavior of the photoemission process leads to a strong increase of the PEEM yield when the two pulses interfere constructively in space and time. For the situation here, we determine a nonlinearity of $N = 3.5 \pm 0.1$ in a single-pulse power-law experiment, i.e., a peak-to-background ratio of 64:1 is expected in the interferometric experiment, which is in concurrence with our experimental observation in Fig. 3b. The results of the actively stabilized TR-PEEM, together with data modeling and simulation, allow retrieving the local system response, which is, in general, strongly dependent on the excitation frequency.[41] This dependency is accessible with our setup, because the interferometer is applicable for tunable laser pulses from the NOPA throughout the VIS regime.

C. Femtosecond pulse shaping and 2D spectroscopy

Figure 4 shows the possibilities of using amplitude- and phase-shaped femtosecond pulses (Fig. 4a) generated by a liquid-crystal-based pulse shaper of our own design to probe the local response of surface systems. The investigated structures (Fig. 4b) are Fabry–Pérot-like plasmonic nanoslit resonators which are cut with defined geometrical length L, width w, and height h into a single-crystalline gold flake by focused-ion-beam milling.[42–44] We detect the spatially resolved photoemission of electrons within single nanoslit resonators generated by plasmon-induced local near-fields with spatial variations on a sub-10 nm length scale using, first, spectrally cut

femtosecond pulses and, second, three-pulse sequences with tunable time delay and controlled relative inter-pulse phase combinations.

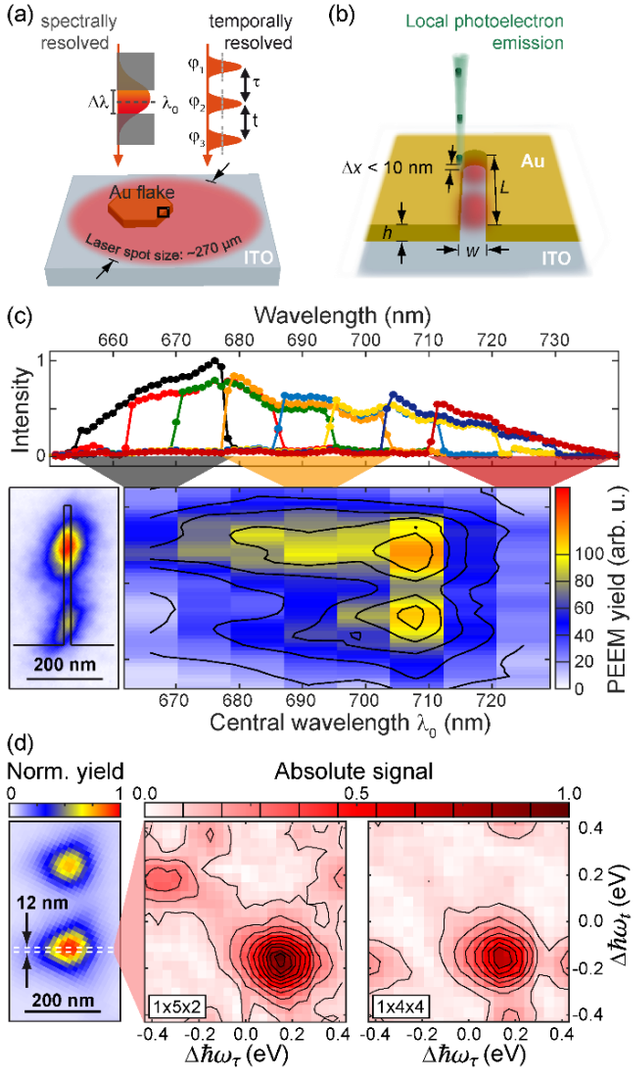

Fig. 4. Application of amplitude- and phase-shaped pulses to probe the local response of plasmonic slit resonators. (a) Scheme of experimental configurations: Pure amplitude shaping (left) generates narrow spectral windows with effective central wavelength $\boldsymbol{\lambda_0}$ and spectral width $\boldsymbol{\Delta\lambda}$ for spectrally selective excitation of the sample. Right: Collinear three-pulse sequence with controlled inter-pulse time-delays $(\boldsymbol{t}, \boldsymbol{\tau})$ and relative inter-pulse phase $\boldsymbol{\varphi_n}$ of each pulse, $\boldsymbol{n = 1, 2, 3}$, by amplitude and phase shaping for coherent 2D nanoscopy. (b) Plasmonic slit resonators with height *h*, width *w,* and length *L* are cut by focused-ion-beam-milling in single-crystalline Au flakes on an indium–tin–oxide-(ITO-)covered glass substrate. Upon laser excitation, high local near-fields (red) of plasmonic modes lead to a characteristic

photoelectron emission pattern (green). (c) Spectrally resolved excitation: Spectra of amplitude-shaped excitation pulses used for static photoelectron emission (top). Bottom left: PEEM image of a slit resonator without spectral narrowing (for geometrical and laser parameters see Fig. 5c). Bottom right: Spatially (line profile along slit) and spectrally resolved photoemission yield as a function of the effective central wavelength λ_0 indicates different resonance properties of the upper and lower hot spots. (d) Left: Laser-induced (660 nm, 19 fs, 56 nJ) photoemission hot spots of a single nanoslit with L = 320 nm, w = 18 nm, and h = 32 nm. Middle and right: Local coherent 2D nanoscopy spectra from an integrated region of interest of 12 nm width (white dashed lines on the left) within one hot spot. The absolute-valued part of the photon-echo contribution after 10-fold (1×5×2, middle) and 16-fold (1×4×4, right) phase cycling is shown. The higher-order contribution in the upper left quadrant of the 2D spectrum with 10-fold phase cycling is eliminated by the 16-fold phase-cycling scheme.

In the first type of experiment, shown in Fig. 4c, eight different spectral windows with the same energy bandwidth are cut out from a NOPA spectrum centered at 700 nm by pure amplitude shaping with our pulse shaper. On the bottom left, the spatial distribution of the detected photoemission pattern is shown for a single nanoslit (geometry indicated in black) exposed to the full laser excitation spectrum and reveals two characteristic emission hot spots. Recording the photoemission yield for eight different spectral windows with effective central wavelength λ_0 and evaluating line profiles along the long slit axis (Fig. 4c, bottom right) shows the different yield contributions to the spectrally integrated spatial yield distribution on the left. The PEEM yield contribution of the lower hot-spot feature is decreased compared to the upper hot spot for the region of λ_0 = 660–690 nm. This indicates that the local response of the upper and lower hot spot varies, i.e., different resonance properties are present at the two hot-spot locations.

By performing independent amplitude and phase shaping with our pulse shaper we generate interferometrically stable collinear three-pulse sequences.[45,46] As depicted in Fig. 4d (left), we

detect the spatially resolved photoemission pattern within a different plasmonic nanoslit of geometrical length L = 320 nm, w = 18 nm, and h = 32 nm, illuminated by a three-pulse sequence with zero inter-pulse time delays and relative phases. By measuring the spatially resolved photoemission yield as a function of both time delays (t, τ) and 2D Fourier transforming the obtained two-dimensional dataset along t and τ, we generate a local 2D nanoscopy spectrum. In contrast to conventional coherent 2D spectroscopy with non-collinear propagation of the exciting pulses and detection of a coherently emitted signal in a phase-matched direction, here, due to our collinear excitation scheme and population-based signal detection (photoelectrons), we filter certain signal contributions, e.g., photon-echo, by using the phase-cycling technique.[47–49] With our pulse shaper we apply for each time delay a combination of different relative inter-pulse phases φ_n. To extract exclusively the rephasing photon-echo contribution in a three-pulse basis, for example, a 10-fold phase-cycling scheme (1×5×2) has been shown to be sufficient in the case that only up to two field interactions per pulse are present, i.e., higher-order effects can be neglected.[47] In Fig. 4d (middle) we show a local 2D spectrum which was integrated over a sample region of interest with 12 nm height (white dashed lines on the left) within a single nanoslit using 1×5×2=10-fold phase cycling. We assign the dominant peak of the absolute signal in the lower right quadrant of the 2D spectrum to the rephasing photon-echo contribution. Since the measurement was performed in a partly rotating frame[45] the absolute signal energy in the laboratory reference frame, $\hbar\omega_{\mathrm{lab}}$, is given by

$$\hbar\omega_{\mathrm{lab},x} = (1-\gamma) * \hbar\omega_0 + \Delta\hbar\omega_x, \qquad (1)$$

with $\hbar\omega_0 = 1.88$ eV corresponding to the central wavelength of the excitation spectrum, $\gamma = 0.1$, and $x \in \{\tau, t\}$. From this equation it is seen that the dominant peak at $|\Delta\hbar\omega_x| = 0.17$ eV appears within our laser spectrum (1.79–1.99 eV). We further detect an additional signal peak in the upper

left quadrant ($\Delta\hbar\omega_\tau = -0.39$ eV, $\Delta\hbar\omega_t = +0.22$ eV), which we assign to a signal contribution of higher order which is not suppressed by the 10-fold phase-cycling scheme. The presence of higher-order signals is reasonable in this sample system, taking into account the nonlinear order of the photoemission process of $N = 3.5$. Since it is expected that a higher phase-cycling scheme suppresses this higher-order contribution we performed an additional three-pulse scan with 1×4×4=16-fold phase cycling. The resultant local 2D nanoscopy spectrum integrated from the same spatial position is shown in Fig. 4d (right) and the signal peak assigned to the higher-order contribution in the upper left quadrant is successfully suppressed. In addition to the expected photon-echo contribution in the lower right quadrant ($|\Delta\hbar\omega_x| = 0.17$ eV), two weaker signal peaks at higher relative energies can be distinguished, which we attribute to remaining higher-order contributions specific to the 16-fold phase-cycling scheme. To further simplify the 2D spectrum, i.e., to suppress these higher-order signal peaks, 1×5×4=20-fold phase cycling would be sufficient. Thus, the possibility to shape femtosecond pulses in amplitude and phase with our pulse shaper extends the PEEM setup to realize spectrally resolved excitation and enables coherent 2D nanoscopy using phase cycling.

D. Photoemission electron microscopy (PEEM)

Figure 5a shows the design of the UHV chamber including the PEEM (left, 4×10^{-11} mbar base pressure) and two-part preparation chamber (right, 5×10^{-10} mbar base pressure). Samples are introduced into the UHV environment via one of two load locks for either direct access to the PEEM or to the preparation chamber. In between there is an additional interconnecting chamber (4×10^{-11} mbar base pressure) with a five-fold sample storage cabinet. The electron microscope was developed and manufactured by Elmitec Elektronenmikroskopie GmbH (AC-LEEM III) and combines the two techniques of PEEM and low-energy electron microscopy (LEEM). For the

latter, electrons are generated from a Schottky-type field emitter and guided to the sample. Emitted (PEEM) or reflected (LEEM) electrons are collected by a system of magnetic lenses in the imaging column. Here, a mirror-type aberration corrector accounts for the principal contributions of spherical and chromatic aberrations introduced mainly by the objective lens.[2–4] A hemispheric imaging energy filter selects electrons by kinetic energy ($\Delta E_{min} \approx 100$ meV) that are detected with a combination of a chevron-type micro-channel plate array with phosphor screen and a CCD camera. In combination, the electron microscope offers a variety of application modes: kinetic-energy-selective imaging in real space (AC-PEEM/LEEM mode) and reciprocal space (spatially selective low-energy electron diffraction μ-LEED, photoelectron diffraction, momentum microscopy), as well as direct imaging of the energy filter's dispersive plane (area-selective spectroscopy). Besides excitation with pulsed laser radiation a continuous-wave Hg discharge lamp (LOT QuantumDesign, LSH102) is used for steady-state photoemission microscopy.

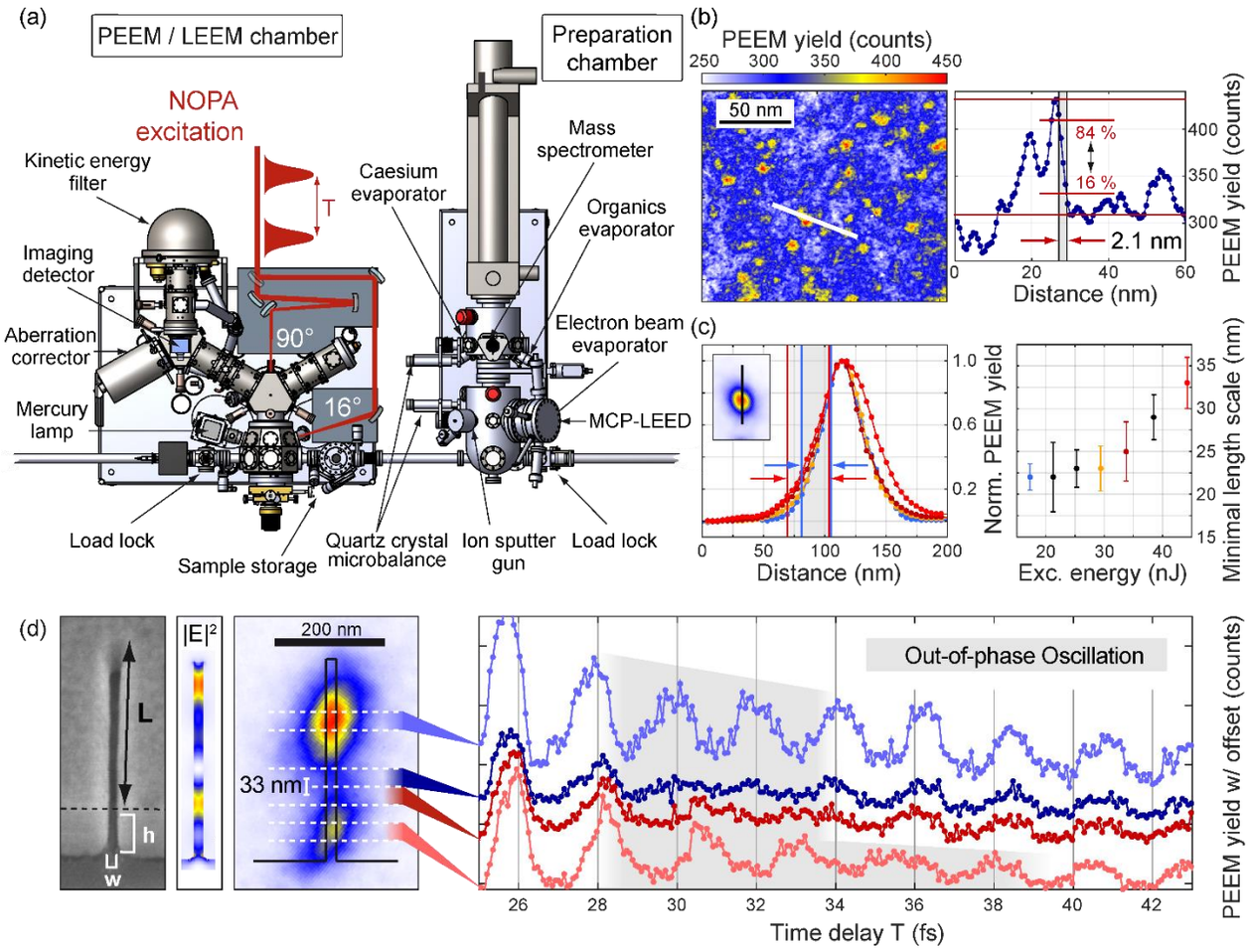

Fig. 5. Setup for time-resolved photoemission electron microscopy with nanometer spatial resolution. (a) Design of the UHV chamber for sample preparation (right) and AC-PEEM (left) with laser beam paths for normal (90° to sample surface) and gracing angle (16°) optical excitation. (b) Photoemission micrograph (top) of lead islands on Si(111) using continuous-wave illumination light (4.9 eV) of a mercury discharge lamp. The topology profile along the white line is shown in the bottom with pixel amplitudes (blue dots) and the extracted spatial resolution (grey shading). (c) Photoemission yield profiles (left) of a particular hot spot of a slit resonator (inset) to characterize the minimum length scale (right) on which characteristic changes in the photoemission yield can be determined as a function of the laser excitation energy (660 nm, 19 fs). (d) From left to right: Scanning electron image of a gold slit resonator with the geometric length L = 360 nm, height h = 31 nm, and width w = 19 nm; simulated distribution of the electric field intensity with the finite-difference time-domain (FDTD) method; spatial distribution of photoemission yield upon illumination with pulsed radiation (700 nm, 22 fs, 12 nJ) in normal-incidence geometry with horizontal dashed white lines defining regions of interest marked in dark and light blue as well as dark and light red; time-delay-dependent PEEM signal for the regions of interest.

The preparation chamber is divided in two parts designated to the preparation of (in-)organic molecular (upper part in Fig. 5a) and metallic thin films (lower part) using physical vapor deposition techniques. A home-built organic-material effusion cell, a commercial electron beam evaporator (Focus, EFM 3), and a Cs evaporator (Elmitec) are available. The deposition rate is monitored during the evaporation process with quartz crystal microbalances (Inficon AG, SQM-160). A quadrupole mass spectrometer (Pfeiffer Vacuum GmbH, Prisma plus) monitors residual gas concentrations from 1 to 200 amu. The quality of long-range ordered surfaces is monitored and controlled with a micro-channel plate (MCP) LEED (Scienta Omicron GmbH, MCP2-LEED) and crystal surfaces are cleaned with an Ar-ion sputtering gun (Omicron, ISE 5). Cooling of the sample stage is possible in the preparation chamber with liquid nitrogen and in the sample storage cabinet as well as in the electron microscope with liquid helium.

The steady-state spatial resolution of the AC-PEEM device is demonstrated in Fig. 5b at Pb islands on Si(111) illuminated with the Hg discharge lamp. We determine the resolution by taking an intensity profile over the rough sample topology and evaluating a steep edge feature according to the 16%–84% criterion.[50] Five profiles are evaluated at different locations from which we determine a spatial resolution of (2.6 ± 0.4) nm, while the smallest detected value is 2.1 nm.

As seen in Fig. 5c, the minimum length scale on which characteristic changes in the photoemission yield are determined depends on the used sample and the applied optical excitation source. Especially for ultrashort laser pulse excitation, space-charge effects might limit the minimum observable length scale. We characterize this effect by recording PEEM images as a function of

excitation pulse energy. Similar to the procedure for retrieving the steady-state spatial resolution, we then obtain a value characterizing the minimum observed length scale from the 16%–84% criterion applied to the image intensity profile of a step-edge feature. Figure 5c shows that the minimum length scale upon laser excitation (660 nm, 19 fs) of this particular hot spot from a slit resonator is ~22 nm (< 35 nJ) and increases for higher excitation energies up to 35 nm. In previous work, we had demonstrated a minimum length scale of 12 nm using fs pulse excitation.[51] Note that the reported minimum length scale does not directly report the spatial resolution but represents only an upper bound, as the physical properties of electric near-field variation determine the spatial rate of change in the recorded image along with the actual resolution.

In contrast to this steady-state resolution, for time-resolved experiments the smallest distances along which local differences of sample dynamics are observed is of interest and is estimated in the following. Figure 5c shows the result of a TR-PEEM experiment using phase-coherent pulse pairs (700 nm, 22 fs, 12 nJ for each pulse) on the same slit-shaped plasmonic resonator, fabricated from single-crystalline Au on an ITO glass slide, as in Fig. 4c. Laser pulses with polarization set perpendicular to the long slit axis excite a localized plasmonic mode in coincidence with finite-difference time-domain simulations, showing the calculated local field intensity (second column in Fig. 5c) and the single-pulse multiphoton photoemission image (third column in Fig. 5c). The two distinct emission features originate from the interplay of the plasmonic excitation and interference with the external field. Interestingly, the hot-spot dynamics, i.e., the local PEEM signal as a function of the inter-pulse delay T (light blue and light red in Fig. 4c, right), shows out-of-phase oscillatory behavior in the range of 28 fs < T < 39 fs. Moreover, evaluating the dynamics of two cross-line locations *in between* the two main hot spots (dark blue and dark red), the same

out-of-phase oscillation is visible. The mean spatial distance between the evaluated locations is 33 nm which we define as the spatial resolution of local dynamics.[52] However, smaller values might be possible depending on sample and excitation properties and are ultimately limited by the steady-state resolution.

For inter-pulse delays smaller than 28 fs the signal is still dominated by the autocorrelated excitation pulses leading to the in-phase oscillatory behavior, whereas for larger delays the signal is mainly influenced by the complex response function of the plasmonic slit resonator. We showed previously that this influence leads to local variations of quantities that are commonly considered to be global properties of a resonator mode such as, e.g., the resonance frequency.[51]

E. Two-color experiments

So far, PEEM experiments using one NOPA output have been discussed. In the following we demonstrate two-color pump–probe PEEM with our experimental setup using simultaneous emission from both NOPA outputs on a monolayer of the transition metal dichalcogenide (TMDC) WSe_2 unraveling local variations of the ultrafast carrier dynamics. This material class, in particular, is very interesting due to the large exciton binding energies up to hundreds of meV,[53,54] making excitonic effects dominant over the semiconductor's response.[55]

We photoexcite the sample with 700 nm (1.77 eV) visible pulses from the 1ω NOPA output above the A-exciton absorption energy and probe the excited-state population via PEEM with time-delayed 290 nm (4.28 eV) UV pulses, delivered from the 2ω NOPA and SHG. The normal-incidence excitation scheme with inter-pulse delay T is indicated in Fig. 6a and the PEEM image of the sample is shown for T = 563.3 fs in Fig. 6b. To compare the ultrafast dynamics, we define

red and blue polygon-shaped regions of interest for the WSe_2 monolayer (bright areas in Fig. 5b) and Si substrate, respectively. The spatially integrated and normalized signal over these regions of interest is plotted as a function of pump–probe time delay in Fig. 5c. While the substrate-related excess signal (blue) vanishes within ~100 fs after photoexcitation, the monolayer signal persists longer.

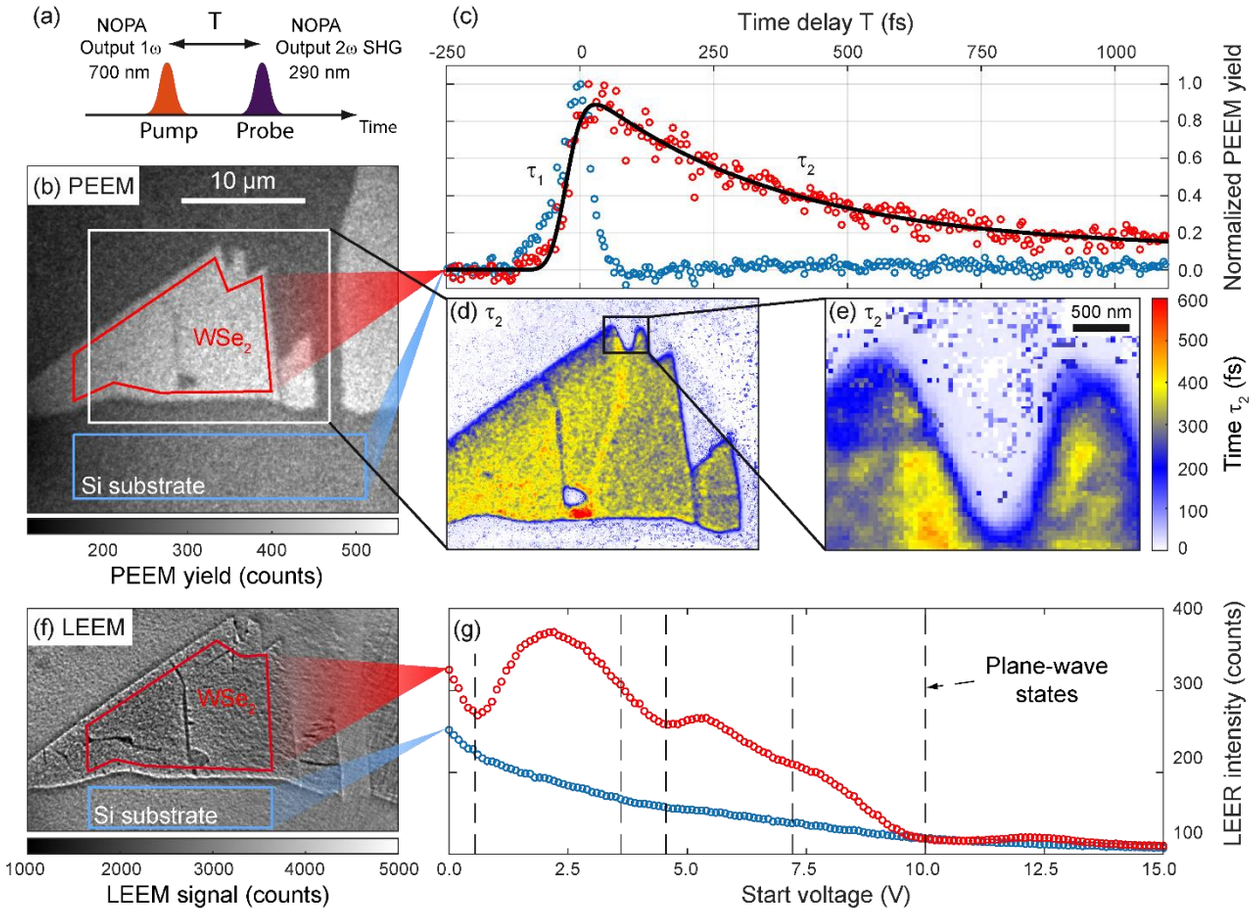

Fig. 6. Two-color pump–probe photoemission microscopy of a monolayer WSe_2 exfoliated on Si(100). (a) Excitation pulse scheme with a visible pump pulse (700 nm) and UV photoemission pulse (290 nm) simultaneously generated by the two NOPA outputs. (b) PEEM image of the WSe_2 monolayer with pulsed laser illumination and a pulse delay of $T \sim 560$ fs. Polygons indicate regions of interest of the WSe_2 (red) and Si substrate position (blue) leading to (c) the normalized integrated photoemission yield as function of time delay T. The black solid line represents the fitting result to the WSe_2 data from which the time constants

$\boldsymbol{\tau_1}$ and decay time $\boldsymbol{\tau_2}$ are extracted. Pixel-by-pixel fitting yields spatial maps of (d) local decay times with (e) a close-up of a local edge feature. (f) Image from low-energy electron microscopy (LEEM) with region-of-interest color definition as in (b). (g) Low-energy electron normal reflectivity (LEER) as a function of sample bias voltage averaged over the WSe_2 (red) and the Si substrate location (blue). Dashed vertical lines indicate positions of plane-wave states extracted from Barrera *et al.*[56], taking into account a work-function offset of 0.34 V in our experimental setup.

To quantify our observations, we adopt a model of Hein *et al.*[57] and deduce characteristic rise and decay times by piece-wise fitting of the following model function:

$$I(T) = I_0 \text{ for } T < t_o, \tag{2}$$

$$I(T) = A_1 \exp\left(-\frac{T - t_o}{\tau_1}\right) + A_2 \exp\left(-\frac{T - t_o}{\tau_2}\right) + I_{\text{residual}} \text{ for } T \geq t_o. \tag{3}$$

Here, $A_1 < 0$ and $A_2 > 0$ account for the build-up and decay of the photoemission signal with time constants τ_1 and τ_2, respectively. I_0 is the overall signal prior to the pump–probe pulse overlap and I_{residual} accounts for excess photoemission signal present at the maximum delay time $T_{\text{max}} =$ 1.1 ps. The condition $I_0 = A_1 + A_2 + I_{\text{residual}}$ guarantees continuity at t_o, which marks the onset time defining the beginning of the build-up of the photoemission signal. To account for finite pulse durations, a Gaussian instrument response function with a full width at half maximum of 50 fs is convoluted with the model function and data are fitted with the varying parameters $t_o, A_1, \tau_1, A_2, \tau_2$, and I_{residual}. The fitting result is shown in Fig. 6c (black solid line) for the spatially integrated monolayer signal and demonstrates good consensus with the experimental data.

Information about local dynamics is obtained by analyzing, in an analogous fashion, the time traces for all pixels individually within the region of interest indicated in white in Fig. 6b. The resulting

map of local decay times in Fig. 6d and as close-up in Fig. 6e, shows variations across the monolayer flake in the range of $300\,\text{fs} < \tau_2 < 600\,\text{fs}$ and indicates a persistently faster depopulation of $\tau_2 \sim 200\,\text{fs}$ at the outer monolayer rims and at crack-like defects. Our results are in accordance with recent PEEM measurements on WSe_2 monolayers grown by chemical vapor deposition, where also a clear spatial dependence of the dynamics has been found on a sub-micrometer scale.[58]

Wang *et al.* interpret the first time constant τ_1 as the time scale of electrons scattered away from the Γ point (out of the probe window) to lower energy regions of the conduction band, since at negative time delays the dynamics are induced by the UV pulse and sampled by the visible pulse. The model introduced by Hein *et al.* correlates the first time constant with an increasing population of excited states. To unambiguously determine the physical meaning of τ_1, the influence of the instrument response function (IRF) on the signal is crucial. Due to the short time scale of $\tau_1 \sim 10 - 30\,\text{fs}$, which is on the order of the pulse duration, we cannot entirely exclude that in our experiment the IRF is the dominant factor at negative delays. This makes an interpretation of the first time constant difficult. Local differences in the IRF will also influence the local behavior of the short time constant.

In contrast, the time constant for positive delays τ_2 is not dominated by the IRF due to their long decay time and maps a decreasing population of the excited states, which has been assigned by Wang *et al.* to electron cooling via intervalley scattering.

However, to identify the exact origin of this effect in our WSe_2 monolayers, which were micromechanically exfoliated from a bulk crystal, a detailed study is necessary, which goes beyond the scope of the present manuscript.

F. Low-energy electron microscopy (LEEM) and reflection (LEER)

In addition to time-resolved PEEM, in our setup static imaging with LEEM yields complementary information about the sample topology, as shown in Fig. 6f for the WSe_2 monolayer sample. Here, mirror-mode LEEM of the monolayer yields images of higher resolution compared to the TR-PEEM experiment in Fig. 6b. The combination of both techniques in a single experimental setup allows us to directly correlate the sample topology, detected with LEEM, to its local carrier dynamics. For example, Fig. 6f shows a structural crack-like defect in the center of the WSe_2 flake which coincides with the position of decreased decay time τ_2 in Fig. 6d, respectively.

In addition to LEEM imaging, we obtain spectroscopic information of the sample under study by measuring the intensity of elastically reflected electrons as a function of the incidence electron kinetic energy, a technique called low-energy electron reflectivity (LEER).[56,59,60] In thin-film materials like graphene and transition metal dichalcogenides, the layer confinement of electrons leads to quantum-well states with energy spacing depending on the film thickness.[56,60] In the LEER experiment, incident electrons can couple resonantly to unoccupied quantum-well states, i.e., conduction bands with the wave vector perpendicular to the film, and experience a decreased reflection probability. These distinct reflection minima result in a fingerprint for a given material and integer number of monolayers, which we can examine with high resolution in our setup. Figure 6g shows LEER spectra for the regions of interest located on the WSe_2 and Si substrate as indicated in Fig. 6f in red and blue, respectively. The local electron reflection signal is spatially integrated and plotted as a function of the positive sample bias voltage, which controls the incidence electron kinetic energy. While for the Si location the signal decreases monotonically for increasing sample bias, an oscillatory behavior is visible for the monolayered WSe_2 signal. For comparison, dashed

vertical lines in Fig. 6g indicate the energy positions of bulk WSe_2 bands with strong in-plane character at the A-point of the Brillouin zone from Barrera *et al.*[56] and taking into account a work function offset of our electron emitter of 0.34 eV in this experiment. The coincidence with the minima in the LEER signal illustrates the spectroscopic features obtained for the WSe_2 sample region. The combination of LEEM and LEER with (multicolor) time-resolved PEEM in our setup offers complementary spectroscopic imaging capabilities in order to unveil structure–dynamics correlations in nanoscaled surface systems.

G. Sample preparation and characterization

In this last subsection we demonstrate the methods of organic thin-film preparation and characterization within the UHV environment of the apparatus. As an example, we prepared a mono-organic thin film of 3,4,9,10-perylenetetra-carboxylic-dianhydride (PTCDA) on an Ag(111) surface via molecular beam epitaxy utilizing a home-built evaporator flanged to the preparation chamber (Fig. 5a, right). We chose the model system PTCDA on Ag(111) because of its well-known arrangement in the long-range ordered herringbone superstructure (Fig. 7a).[61–64] Due to the hexagonal symmetry of the Ag(111) surface, the PTCDA unit cells arrange in six symmetry-equivalent rotational domains.[61,62] For the preparation of the sample, the Ag(111) crystal was first put through several sputtering and annealing cycles before PTCDA deposition at 623 K onto the substrate at 300 K and subsequent sample annealing at 543 K for 10 min. The growth of the organic thin film induces a characteristic change of the diffraction pattern, which we observe with MCP-LEED directly in the preparation chamber, i.e., no transfer to the PEEM main chamber (Fig. 5a left) is required and thus time-efficient sample preparation and characterization cycles are feasible. In contrast to conventional LEED setups, the high sensitivity of MCP-detected LEED allows for low primary electron currents in order to keep the impact of electron bombardment as low as possible, which is helpful in particular for organic thin-film preparation.

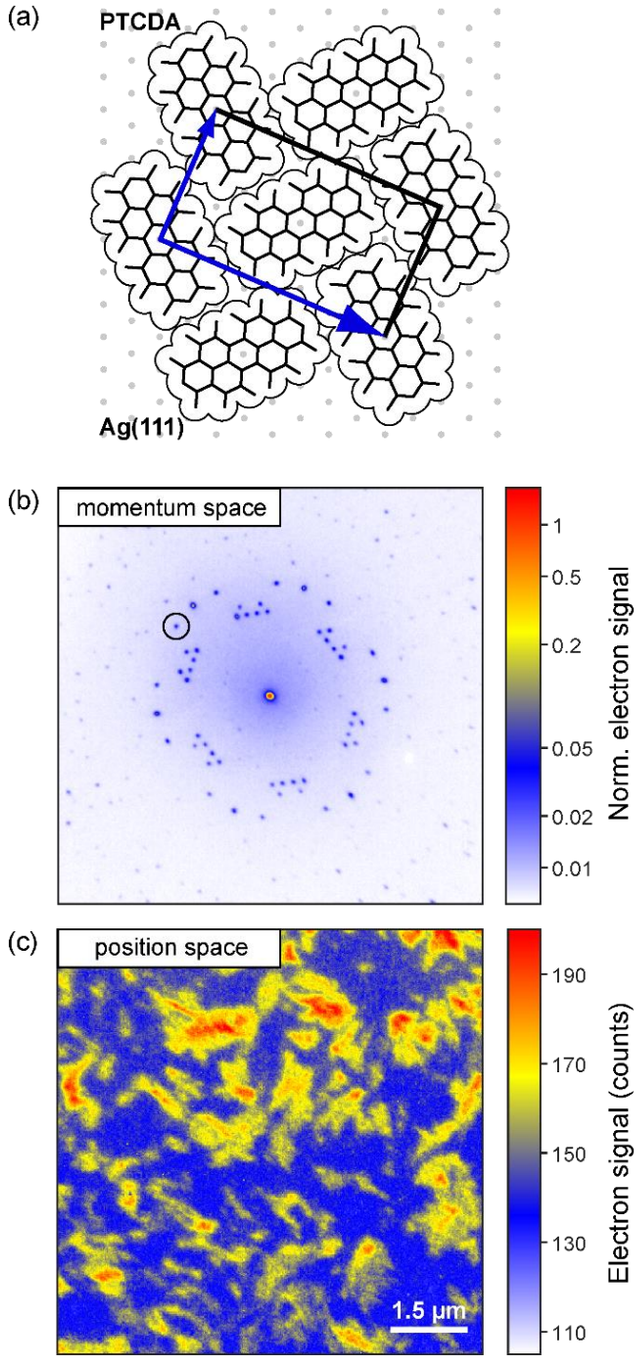

Fig. 7. Mono-organic thin film of 3,4,9,10-perylenetetra-carboxylic-dianhydride (PTCDA) on Ag(111). (a) Hard-sphere model of the lateral adsorption geometry of the PTCDA unit cell, spanned by the blue arrows, in a herringbone superstructure.[61,62] (b) Spatially resolved low-energy electron diffraction (µ-LEED) pattern of PTCDA/Ag(111). The black circle indicates a diffraction spot corresponding to a single adsorption conformation which is filtered to obtain (c) a dark-field low-energy electron microscopy (LEEM) image.

In contrast to MCP-LEED, which is a spatially integrating technique, it is possible to examine micrometer-sized areas of the sample with μ-LEED in the main chamber. Figure 7b shows the detected characteristic μ-LEED pattern of long-range ordered PTCDA thin films on Ag(111) in the herringbone superstructure. By filtering the signal of a single diffraction spot in the back focal plane (black circle in Fig. 7b) for dark-field LEEM imaging, we image the coverage of a single associated symmetry-equivalent rotational domain in real space (Fig. 7c). In molecular adsorbates, the orientation of the rotational domains defines the direction of the molecular dipole moment, i.e., the susceptibility to external (linearly polarized) light fields and thus, in general, alters the local molecular dynamics detected with TR-PEEM for the different domains. Thus, this method can provide additional information for interpreting molecular 2D nanoscopy experiments, for example, by revealing the dipole orientation with respect to the excitation pulse sequence.

III. CONCLUSION

To summarize, we introduce a versatile setup for time-resolved aberration-corrected photoemission electron microscopy (TR-AC-PEEM) that facilitates down to 3 nm spatial resolution in combination with laser excitation by a broadband tunable (215–970 nm) sub-20-fs pulsed light source at 1 MHz repetition rate. Phase-coherent pulse trains from an actively phase-stabilized interferometer and LCD-based pulse shaping were applied and we demonstrated single-pulse spectroscopy, single-color pump–probe as well as coherent 2D nanoscopy experiments on plasmonic Au nanostructures. In general, it is not possible to observe the maximum device resolution with an arbitrary sample upon pulse laser excitation.[5] Here we determine characteristic changes of the photoemission signal across a minimum length scale of a photoemission hot spot in a plasmonic nanoslit resonator of about 22 nm, reflecting a mixture of the underlying physics

of the sample and the actual (lower) device resolution of 3 nm. Note that the PEEM/LEEM system has an energy analyzer that allows us to acquire kinetic energies of electrons in addition to spatial, temporal, and (multi-dimensional) optical energy resolution. Further, we mapped local differences of the population dynamics in the TMD material WSe_2 in a two-color pump–probe scheme from two independently tunable NOPA beamlines.

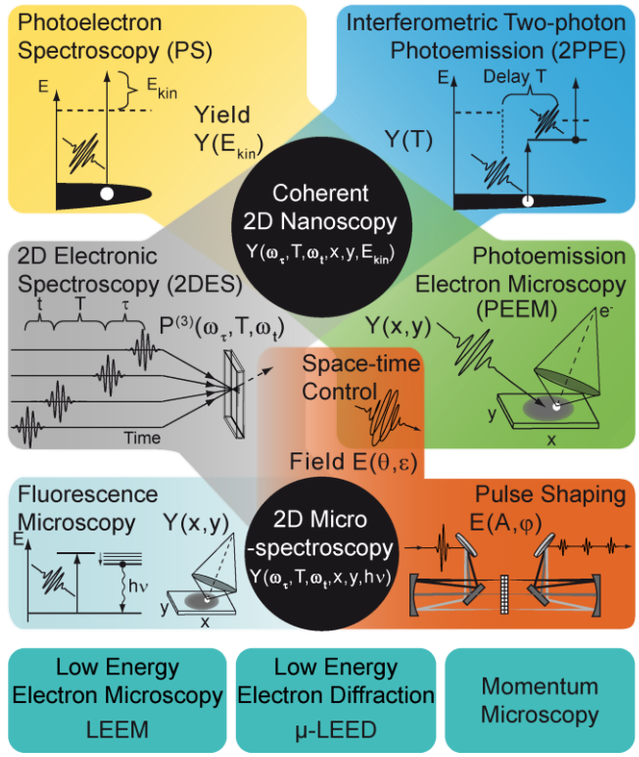

Fig. 8. Schematic overview of the available methods and techniques with the presented experimental setup. Broadband tunable laser excitation (215–970 nm) at 1 MHz repetition rate and sub-20 fs pulse duration is realized via the dual-output NOPA system. By combining photoemission electron microscopy (PEEM, ultimate imaging resolution 3 nm) with photoelectron spectroscopy (PS, kinetic energy resolution ~100 meV), interferometric two-photon photoemission (2PPE) and 2D electronic spectroscopy (2DES), we perform coherent 2D nanoscopy. Despite the incoherent observation of the electron yield $\boldsymbol{Y(\omega_\tau, T, \omega_t, x, y, E_{kin})}$, phase cycling allows us to disentangle the local nonlinear optical coherence information. The required femtosecond multipulse sequences are generated by amplitude and phase shaping of the electric field $\boldsymbol{E(A, \varphi)}$. Phase- and polarization-shaped (future option) pulses $\boldsymbol{E(\theta, \epsilon)}$ enable space–time control of nanooptical near-fields.[65] Instead of photoelectrons, using the sample's local fluorescence

yield $\boldsymbol{Y(\omega_\tau, T, \omega_t, x, y, h\nu)}$ as incoherent observable gives rise to surface system investigations by 2D micro-spectroscopy[33] (future option not discussed further in the present work). Additional surface-sensitive techniques such as μ-LEED, LEEM (ultimate imaging resolution < 3 nm) and momentum microscopy allow a detailed and comprehensive investigation of the physical surface properties which yield complementary insights in the sample of study.

Figure 8 summarizes the different modalities of the presented apparatus that combines versatile techniques of surface (electron) microscopy (PS, 2PPE, PEEM) with coherent two-dimensional electronic spectroscopy (2DES) realizing the performance of coherent 2D nanoscopy experiments. We measure the spatially resolved incoherent electron yield $Y(\omega_\tau, T, \omega_t, x, y, E_{kin})$ to probe the nonlinear sample coherence on the nanoscale. Using amplitude- and phase-shaped pulse sequences $E(A, \varphi)$ certain contributions to the local nonlinear optical coherence information can be disentangled by the phase-cycling technique. This enables us to investigate, e.g., the dominating mechanisms of energy transport in surface systems. As demonstrated earlier,[65] advanced control of the excitation field $E(\theta, \epsilon)$ by phase and polarization pulse shaping (the latter is an option planned for the future) extends the versatility to space–time control of nanooptical near fields at the sample and thus to optically induced modifications of the environmental coupling. Complementing investigations by using the sample's fluorescence yield $Y(\omega_\tau, T, \omega_t, x, y, h\nu)$ as incoherent observable via 2D micro-spectroscopy[33] and surface-sensitive techniques such as μ-LEED, LEEM and momentum microscopy allow a detailed *ex vacuo* and *in vacuo* characterization of the investigated surface system.

Together with the capability of in-situ preparation of (in-)organic thin films, here exemplified on PTCDA/Ag(111), our setup offers vast possibilities to investigate, e.g., molecular surface systems and hybrid nanostructures with coherent multidimensional nanoscopy and multicolor excitation schemes.

AUTHOR INFORMATION

Corresponding Author

*E-mail: brixner@phys-chemie.uni-wuerzburg.de

OrcId:

Bernhard Huber: 0000-00002-5472-8596

Matthias Hensen: 0000-0002-5578-0118 381

Tobias Brixner: 0000-0002-6529-704X

Bert Hecht: 0000-0002-4883-8676

Sebastian Pres: 0000-0002-8402-4864

Daniel Fersch: 0000-0002-0570-0212

Emanuel Wittmann: 0000-0001-5022-0851

Eberhard Riedle: 0000-0002-2672-5718

Author Contributions

T.B. initiated the project. T.B., B.He., M.H., E.R. and R.B. initiated and supervised the experiments. L.D., D.Fe., M.H., B.Hu., V.L., J.L. and S.P. assembled the experimental setup. In particular D.Fe. built the fluorescence microscope. B.Hu. planned the LEEM-PEEM setup. J.L. built the phase-stabilized interferometer. S.P. built the liquid-crystal-based pulse shaper. E.W. built the NOPA. D.Fr. and E.K. designed the plasmonic nanoslits and prepared the sample. Further, D.Fr. and E.K. performed the SEM characterization measurements. J.K. prepared the WSe_2 sample. B.Hu, V.L., S.P. and E.W. performed the NOPA characterization measurements. B.Hu., D.Fe. and S.P. performed the pulse-shaper measurements. B.Hu., M.H. and S.P. performed the

single-color time-resolved PEEM measurements on the plasmonic nanoslit sample. B.Hu. and V.L. performed the multicolor time-resolved PEEM and LEEM/LEER measurements on WSe_2. B.Hu., L.D. and S.P. performed the PTCDA preparation and characterization measurements. B.Hu., L.D. and S.P. wrote the manuscript with input from all coauthors. B.Hu. and S.P. contributed equally to this work. All authors contributed to the discussion and have given approval to the final version of the manuscript.

Notes

The authors declare no competing financial interest.

ACKNOWLEDGMENT

We acknowledge fruitful discussions and technical support by Elmitec GmbH. T.B. gratefully acknowledges financial support from the European Research Council (ERC Consolidator Grant "MULTISCOPE" – No. 614623).

REFERENCES

[1] G.D. Scholes, G.R. Fleming, L.X. Chen, A. Aspuru-Guzik, A. Buchleitner, D.F. Coker, G.S. Engel, R. van Grondelle, A. Ishizaki, D.M. Jonas, J.S. Lundeen, J.K. McCusker, S. Mukamel, J.P. Ogilvie, A. Olaya-Castro, M.A. Ratner, F.C. Spano, K.B. Whaley, and X. Zhu, Nature **543**, 647 (2017).

[2] R.M. Tromp, J.B. Hannon, A.W. Ellis, W. Wan, A. Berghaus, and O. Schaff, Ultramicroscopy **110**, 852 (2010).

[3] E. Bauer, Ultramicroscopy **119**, 18 (2012).

[4] E. Bauer, J. Electron. Spectrosc. Relat. Phenomena **185**, 314 (2012).

[5] E. Bauer, *Surface Microscopy with Low Energy Electrons* (Springer, New York, 2014).

[6] M. Aeschlimann, C.A. Schmuttenmaer, H.E. Elsayed-Ali, R.J.D. Miller, J. Cao, Y. Gao, and D.A. Mantell, J. Chem. Phys. **102**, 8606 (1995).

[7] O. Schmidt, M. Bauer, C. Wiemann, R. Porath, M. Scharte, O. Andreyev, G. Schönhense, and M. Aeschlimann, Appl. Phys. B **74**, 223 (2002).

[8] A. Kubo, K. Onda, H. Petek, Z. Sun, Y.S. Jung, and H.K. Kim, Nano Lett. **5**, 1123 (2005).

[9] M. Cinchetti, A. Gloskovskii, S.A. Nepjiko, G. Schönhense, H. Rochholz, and M. Kreiter, Phys. Rev. Lett. **95**, 047601 (2005).

[10] A. Kubo, N. Pontius, and H. Petek, Nano Lett. **7**, 470 (2007).

[11] F.-J. Meyer zu Heringdorf, L.I. Chelaru, S. Möllenbeck, D. Thien, and M. Horn-von Hoegen, Surf. Sci. **601**, 4700 (2007).

[12] J. Graf, S. Hellmann, C. Jozwiak, C.L. Smallwood, Z. Hussain, R.A. Kaindl, L. Kipp, K. Rossnagel, and A. Lanzara, J. Appl. Phys. **107**, 014912 (2010).

[13] N.M. Buckanie, J. Göhre, P. Zhou, D. von der Linde, M. Horn-von Hoegen, and F.-J. Meyer zu Heringdorf, J. Phys. Condens. Matter **21**, 314003 (2009).

[14] T. Munakata, T. Masuda, N. Ueno, A. Abdureyim, and Y. Sonoda, Surf. Sci. **507**, 434 (2002).

[15] A. Mikkelsen, J. Schwenke, T. Fordell, G. Luo, K. Klünder, E. Hilner, N. Anttu, A.A. Zakharov, E. Lundgren, J. Mauritsson, J.N. Andersen, H.Q. Xu, and A. L'Huillier, Rev. Sci. Instrum. **80**, 123703 (2009).

[16] S.H. Chew, F. Süßmann, C. Späth, A. Wirth, J. Schmidt, S. Zherebtsov, A. Guggenmos, A. Oelsner, N. Weber, J. Kapaldo, A. Gliserin, M.I. Stockman, M.F. Kling, and U. Kleineberg, Appl. Phys. Lett. **100**, 051904 (2012).

[17] S.H. Chew, K. Pearce, C. Späth, A. Guggenmos, J. Schmidt, F. Süßmann, M.F. Kling, E. Mårsell, C.L. Arnold, E. Lorek, P. Rudawski, C. Guo, M. Miranda, and F. Ardana, in *Attosecond Nanophysics* (Wiley-VCH Verlag GmbH & Co. KGaA, 2015), pp. 325–364.

[18] G. Cerullo and S. De Silvestri, Rev. Sci. Instrum. **74**, 1 (2003).

[19] C. Homann, C. Schriever, P. Baum, and E. Riedle, Opt. Express **16**, 5746 (2008).

[20] M. Bradler and E. Riedle, Opt. Lett. **39**, 2588 (2014).

[21] A. Höfer, K. Duncker, M. Kiel, S. Förster, and W. Widdra, IBM J. Res. Dev. **55**, (2011).

[22] M. Dąbrowski, Y. Dai, A. Argondizzo, Q. Zou, X. Cui, and H. Petek, ACS Photonics **3**, 1704 (2016).

[23] M. Dąbrowski, Y. Dai, and H. Petek, J. Phys. Chem. Lett. **8**, 4446 (2017).

[24] A. Sander, M. Christl, C.-T. Chiang, M. Alexe, and W. Widdra, J. Appl. Phys. **118**, 224102 (2015).

[25] S. Tan, L. Liu, Y. Dai, J. Ren, J. Zhao, and H. Petek, J. Am. Chem. Soc. **139**, 6160 (2017).

[26] K. Duncker, M. Kiel, and W. Widdra, Surf. Sci. **606**, L87 (2012).

[27] M. Aeschlimann, T. Brixner, A. Fischer, C. Kramer, P. Melchior, W. Pfeiffer, C. Schneider, C. Strüber, P. Tuchscherer, and D.V. Voronine, Science **333**, 1723 (2011).

[28] A. Mikkelsen, Nat. Photon. **5**, 651 (2011).

[29] C. Schriever, S. Lochbrunner, P. Krok, and E. Riedle, Opt. Lett. **33**, 192 (2008).

[30] A.M. Weiner, Rev. Sci. Instrum. **71**, 1929 (2000).

[31] A. Monmayrant, S. Weber, and B. Chatel, J. Phys. B: At. Mol. Opt. Phys. **43**, 103001 (2010).

[32] C. Homann, N. Krebs, and E. Riedle, Appl. Phys. B **104**, 783 (2011).

[33] S. Goetz, D. Li, V. Kolb, J. Pflaum, and T. Brixner, Opt. Express **26**, 3915 (2018).

[34] E. Wittmann, S. Heimann, and E. Riedle, in *2017 Conference on Lasers and Electro-Optics Europe European Quantum Electronics Conference (CLEO/Europe-EQEC)* (2017), pp. 1–1.

[35] P. Baum, S. Lochbrunner, and E. Riedle, Appl. Phys. B **79**, 1027 (2004).

[36] A.D. Bristow, D. Karaiskaj, X. Dai, T. Zhang, C. Carlsson, K.R. Hagen, R. Jimenez, and S.T. Cundiff, Rev. Sci. Instrum. **80**, 073108 (2009).

[37] V. Volkov, R. Schanz, and P. Hamm, Opt. Lett. **30**, 2010 (2005).

[38] U. Selig, F. Langhojer, F. Dimler, T. Löhrig, C. Schwarz, B. Gieseking, and T. Brixner, Opt. Lett. **33**, 2851 (2008).

[39] D. Brida, C. Manzoni, and G. Cerullo, Opt. Lett. **37**, 3027 (2012).

[40] M.U. Wehner, M.H. Ulm, and M. Wegener, Opt. Lett. **22**, 1455 (1997).

[41] M. Aeschlimann, T. Brixner, A. Fischer, M. Hensen, B. Huber, D. Kilbane, C. Kramer, W. Pfeiffer, M. Piecuch, and P. Thielen, Appl. Phys. B 122 (2016).

[42] E. Krauss, R. Kullock, X. Wu, P. Geisler, N. Lundt, M. Kamp, and B. Hecht, Cryst. Growth Des. (2018).

[43] K. Chen, G. Razinskas, H. Vieker, H. Gross, X. Wu, A. Beyer, A. Gölzhäuser, and B. Hecht, Nanoscale **10**, 17148 (2018).

[44] H. Groß, J.M. Hamm, T. Tufarelli, O. Hess, and B. Hecht, Sci. Adv. **4**, eaar4906 (2018).

[45] A. Galler and T. Feurer, Applied Physics B **90**, 427 (2008).

[46] T. Feurer, J.C. Vaughan, R.M. Koehl, and K.A. Nelson, Opt. Lett. **27**, 652 (2002).

[47] H.-S. Tan, J. Chem. Phys. **129**, 124501 (2008).

[48] P. Tian, D. Keusters, Y. Suzaki, and W.S. Warren, Science **300**, 1553 (2003).

[49] D. Keusters, H.-S. Tan, and W.S. Warren, J. Phys. Chem. A **103**, 10369 (1999).

[50] A.B. Pang, T. Müller, M.S. Altman, and E. Bauer, J. Phys.: Condens. Matter **21**, 314006 (2009).

[51] M. Hensen, B. Huber, D. Friedrich, E. Krauss, S. Pres, P. Grimm, D. Fersch, J. Lüttig, V. Lisinetskii, B. Hecht, and T. Brixner, Nano Lett. **19**, 4651 (2019).

[52] B. Huber, M. Hensen, S. Pres, V. Lisinetskii, J. Lüttig, E. Wittmann, E. Krauss, D. Friedrich, B. Hecht, E. Riedle, and T. Brixner, Web Conf. **205**, 08002 (2019).

[53] M.M. Ugeda, A.J. Bradley, S.-F. Shi, F.H. da Jornada, Y. Zhang, D.Y. Qiu, W. Ruan, S.-K. Mo, Z. Hussain, Z.-X. Shen, F. Wang, S.G. Louie, and M.F. Crommie, Nature Materials **13**, 1091 (2014).

[54] S. Park, N. Mutz, T. Schultz, S. Blumstengel, A. Han, A. Aljarb, L.-J. Li, E.J.W. List-Kratochvil, P. Amsalem, and N. Koch, 2D Mater. **5**, 025003 (2018).

[55] C.L. Smallwood and S.T. Cundiff, Laser & Photonics Reviews **12**, 1800171 (2018).

[56] S.C. de la Barrera, Y.-C. Lin, S.M. Eichfeld, J.A. Robinson, Q. Gao, M. Widom, and R.M. Feenstra, J. Vac. Sci. Technol. **34**, 04J106 (2016).

[57] P. Hein, A. Stange, K. Hanff, L.X. Yang, G. Rohde, K. Rossnagel, and M. Bauer, Phys. Rev. B **94**, 205406 (2016).

[58] L. Wang, C. Xu, M.-Y. Li, L.-J. Li, and Z.-H. Loh, Nano Lett. **18**, 5172 (2018).

[59] J. Jobst, A.J.H. van der Torren, E.E. Krasovskii, J. Balgley, C.R. Dean, R.M. Tromp, and S.J. van der Molen, Nat. Commun. **7**, (2016).

[60] R.M. Feenstra, N. Srivastava, Q. Gao, M. Widom, B. Diaconescu, T. Ohta, G.L. Kellogg, J.T. Robinson, and I.V. Vlassiouk, Phys. Rev. B **87**, 041406 (2013).

[61] K. Glöckler, C. Seidel, A. Soukopp, M. Sokolowski, E. Umbach, M. Böhringer, R. Berndt, and W.-D. Schneider, Surf. Sci. **405**, 1 (1998).

[62] L. Kilian, E. Umbach, and M. Sokolowski, Surf. Sci. **573**, 359 (2004).

[63] E. Umbach, K. Glöckler, and M. Sokolowski, Surf. Sci. **402–404**, 20 (1998).

[64] H. Marchetto, T. Schmidt, U. Groh, F.C. Maier, P.L. Lévesque, R.H. Fink, H.-J. Freund, and E. Umbach, Phys. Chem. Chem. Phys. **17**, 29150 (2015).

[65] M. Aeschlimann, M. Bauer, D. Bayer, T. Brixner, S. Cunovic, F. Dimler, A. Fischer, W. Pfeiffer, M. Rohmer, C. Schneider, F. Steeb, C. Strüber, and D.V. Voronine, PNAS **107**, 5329 (2010).